PAPER • OPEN ACCESS

Genesis of column sprites: formation mechanisms and optical structures

To cite this article: R Marskar 2024 *Plasma Sources Sci. Technol.* **33** 025024

View the article online for updates and enhancements.

Genesis of column sprites: formation mechanisms and optical structures

R Marskar ®

SINTEF Energy Research, Sem Sælands vei 11, Trondheim 7034, Norway

E-mail: robert.marskar@sintef.no

CrossMark

Abstract
Sprite discharges are electrical discharges that initiate from the lower ionosphere during intense lightning storms, manifesting themselves optically as flashes of light that last a few milliseconds. This study unravels sprite initiation mechanisms and evolution into distinctive morphologies like glows and beads, using direct 3D numerical simulations that capture the intricate electrical discharge processes. We clarify various morphological aspects of sprites such as the halo dynamics, column glows, branching, streamer reconnection, and bead formation. The results advance our understanding of sprites and their connection to thunderstorm dynamics, and puts quantitative analysis of their effect on Earth's climate within reach.

Keywords: sprite, streamer, simulation

1. Introduction

The phenomenon known as sprite discharges in the upper atmosphere has captivated scientists and skygazers for decades. Often referred to as red sprites due to their distinctive reddish glow, they manifest as millisecond-short flashes of light high above thunderstorms (40–80 km). The initial inklings of sprite discharges trace back hundreds of years to eyewitnesses reports, while more recent observations have been reported by amateur photographers, pilots, and astronauts. These anecdotal accounts were validated when the first documented evidence was conclusively captured on camera in 1989 [1]. Since then, high-speed photography [2, 3] have unveiled a rich tapestry of sprite activity, establishing sprites as a field of study that offers unique insights into the electrical interactions within Earth's atmosphere. Due to advances in consumer-grade hardware, sprites are now routinely captured also by amateur photographers, as exemplified by the NASA 'Spritacular' citizen science project [4].

Research on sprites transcends scientific curiosity as they emit bursts of radio waves and disrupt the ionosphere, influence the propagation of radio signals, and introduce uncertainties in communication and navigation systems. Furthermore, sprites can generate reactive species in the Earth atmosphere in large quantities and thus affect Earth's long term atmospheric composition. Unraveling the nature of sprite streamers thus holds significant implications for understanding Earth's atmospheric electricity, ionospheric dynamics, and climate.

It is now accepted that sprites originate during intense lightning discharges from thunderstorms, which generate quasi-static electric fields that extend into the upper atmosphere. As the breakdown strength E_{br} of air relative to the number density of neutral molecules N is a constant (i.e. $E_{br}/N \approx 120$ Td in air), and N decreases exponentially with altitude, powerful lightning strikes can initiate electrical breakdown in the upper atmosphere [5]. The quasi-static electric fields that originate in charged thunderclouds do not penetrate the ionosphere as it is sufficiently conductive and, analogous to metals, has no internal electric field on the time scale of sprites. But the fields initiate a cascade of processes at the lower edge of the ionosphere which ultimately lead to the formation a filamentary type of plasma known as streamers [6]. These structures propagate through self-enhanced electric fields at their tips, and can propagate downwards in the atmosphere for tens

Figure 1. True color photo of a large carrot sprite over France. Reproduced with permission from [4]. Courtesy of Nicolas Escurat via the Spritacular citizen project.

of kilometers. The optical emission from sprites result from electron impact excitation and spontaneous emission from the first and second positive system of molecular nitrogen (1PN2 and 2PN2), resulting in the display of red and purple hues that often define sprites.

Most sprite discharges occur during positive cloud-to-ground (+CG) lightning and display a fascinatingly rich morphology, see figure 1. High-speed video studies [7] show that sprites are often preceded by a sprite halo [8–10], which is a large diffuse glow with lateral extents exceeding tens of kilometers. Although halos from +CG and -CG lightning occur with almost the same frequency for a given lightning current [11], virtually all sprites arise from +CG lightning, while negative sprites are rarely seen [12]. Sprites are classified as column or carrot sprites, with the primary difference being that column sprites consist of only downwards propagating streamers and carrot sprites also consist of upwards propagating streamers. Telescopic imaging [13–15] shows that sprite discharges have a fine structure consisting of long-lasting column-shaped glows near the top of the sprite, and occasionally also spots (i.e. beads) along the streamer channels. This optical fine structure dominates long-exposure images of sprites, while the streamer channels leave relatively faint traces, as shown in figure 1.

While sprite discharges have been a subject of scientific scrutiny since their indisputable discovery 35 years ago, many unanswered questions remain. One key mystery pertains to the precise mechanism triggering the formation and morphological structure of sprites [16]. It is widely accepted that they are associated with lightning strikes, but the specific

conditions and processes leading to their creation remain incompletely understood, as are the intricate details of sprites' complex internal structure and behavior. This includes factors that determine their distinctive shapes, sizes, and morphology, such as the breakup of the halo, and the appearance of long-lasting columniform glows and luminous beads. Many of these questions have remained theoretically inaccessible, primarily owing to a lack of appropriate theoretical tools that capture the full three-dimensional evolution of the sprite across the many time and length scales that are involved in their formation.

In this paper we theoretically study, for the first time, the complete three-dimensional formation of a moderately-sized atmospheric column sprite with realistic theoretical models and atmospheric conditions. We track the evolution of the sprite from its inaugural birth in the sprite halo and as it descends in the atmosphere. Our results reproduce many optical signatures associated with sprites, such as (1) the appearance and breakup of an initial halo, (2) downwards shooting positive streamers, (3) streamer branching, (4) sprite glows, (5) streamer reconnections, and (6) sprite beads. We also find that these processes have rather clear physical interpretations and emergence mechanisms.

This paper is organized as follows: In section 2 we discuss the physical and computer models that are used. In section 3 we provide observations of the various stages of the sprite, and provide step-by-step interpretations of their physical mechanisms. We compare our observations with past modeling studies as well as experimental observations wherever possible. Finally, in section 4 we provide a brief summary of the paper.

2. Theoretical model

2.1. Plasma chemistry and evolution

We model the plasma as densities using 3D advection-diffusion-reaction equations for species number densities n_i,

$$\partial_t n_i + \nabla \cdot (\boldsymbol{v}_i n_i - D_i \nabla n_i) = S_i, \qquad (1)$$

where i is some species (e.g. electrons or a type of ion), $\boldsymbol{v}_i = \pm\mu_i \boldsymbol{E}$ is the advective velocity for species with positive (+) and negative (−) charge numbers, μ_i are mobilities, D_i are diffusion coefficients, and S_i are source terms. The electric field $\boldsymbol{E}$ is obtained from the Poisson equation

$$\nabla \cdot \boldsymbol{E} = \frac{\rho}{\epsilon_0}, \qquad (2)$$

where $\rho = \sum_i q_e Z_i n_i$ where q_e is the elementary charge and Z_i are charge numbers. For greatest simplicity, the Earth atmosphere is modeled as a gaseous background of 20% O_2 and 80% N_2, where the temperature T and density ρ are given as functions of altitude z above sea-level as shown in figure 2. We solve the above equations self-consistently for electrons e, ions N_2^+, O_2^+, and O^-, while the relative change in the densities of O_2 and N_2 are ignored as the ionization degree is typically below 10^{-4}. Chemical reactions are given in table 1, and transport data for the electrons are computed using BOLSIG+ [17] and the SIGLO database [18]. Since the transport data

Table 1. Simplified sprite chemistry used in the model. N_2 and O_2 indicate ground states, while optical emission follows from the first positive system $N_2\left(B^3\Pi_g\right) \to N_2$.

#	Type	Reaction	Symbol	References
R_1	Ionization	$e + N_2 \to e + e + N_2^+$	$k_1(E,z)$	[17, 18]
R_2	Ionization	$e + O_2 \to e + e + O_2^+$	$k_2(E,z)$	[17, 18]
R_3	Dissociative attachment	$e + O_2 \to O + O^-$	$k_3(E,z)$	[17, 18]
R_4	Optical emission	$e + N_2 \to e + N_2\left(B^3\Pi_g\right)$	$k_4(E,z)$	[17–19]
R_γ	Photon production	$e + N_2 \to e + N_2 + \gamma$	$k_\gamma(E,z)$	[17, 18, 20]
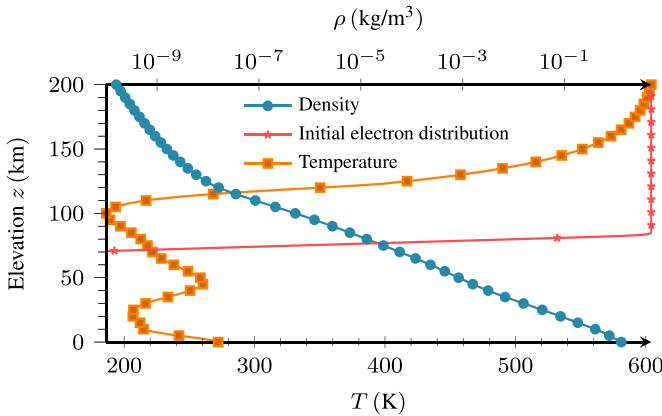
Figure 2. Electron density profile (arbitrary units), and atmospheric gas density and temperature as a function of elevation z. The atmospheric density was computed with an ENMSIS atmospheric model.

only shows minor variations with temperature for 200–300 K, it is computed for a constant temperature $T = 200$ K. Ions are considered as stationary.

2.2. Photoionization

Photoionization is treated using Monte Carlo sampling as in [21, 22], corrected for altitude. For N_2-O_2 mixtures, photoionization of molecular oxygen can occur by electron impact excitation of nitrogen to one of the involved singlet states (denoted by N_2^{exc} below) [19, 23],

$$e + N_2 \to e + N_2^{exc}. \tag{3}$$
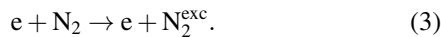
If N_2^{exc} is not predissociated or quenched, the state decays through spontaneous emission $N_2^{exc} \to N_2 + \gamma$ which can lead to photoionization of molecular oxygen:

$$\gamma + O_2 \to e + O_2^+. \tag{4}$$
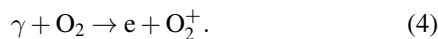
The physical number of photons that are generated per unit time and volume is

$$S_\gamma = k_\gamma n_e n_{N_2} \tag{5}$$

where

$$k_\gamma = \frac{p_q}{p + p_q} \nu_Z(E) k_1. \tag{6}$$

Here, $p = p(z)$ is the gas pressure and $p_q = 40$ mbar is a quenching pressure which describes collisional de-excitation of the various N_2 singlet states [23]. This factor is included, although we point out that the quenching provides a negligible correction at sprite altitudes, but reduces photoionization by approximately a factor of 0.04 at atmospheric pressure. The function $\nu_Z(E)$ is a correction factor that accounts for photoionization probabilities and excitation efficiencies, see Pancheshnyi [24]. The physical number of photons that is generated in each time step Δt in a grid cell with volume ΔV is then sampled as $P(S_\gamma \Delta t \Delta V)$, where $P(\mu)$ is a Poisson distribution with mean value μ. When computational photons are generated we sample the mean absorption length κ_f individually for computational photons with frequency f using

$$\kappa_f = p_{O_2} \chi_{\min} \left(\frac{\chi_{\max}}{\chi_{\min}}\right)^{\frac{f-f1}{f2-f1}}, \tag{7}$$

where p_{O_2} is the partial pressure of oxygen, $\chi_{\min} = 2.625 \times 10^{-2}$ Pa^{-1}m^{-1} and $\chi_{\max} = 1.5$ Pa^{-1}m^{-1}. The photon frequency f is uniformly sampled on the interval $f \in [f_1, f_2]$ where $f_1 = 2.91$ PHz and $f_2 = 3.06$ PHz [19].

Figure 3 shows the calculated maximum and minimum mean absorption lengths in our photoionization model as a function of altitude. In the computer implementation the absorption position of a computational photon is doubly sampled: We first sample f on the specified interval and compute κ_f for each photon, and then sample the propagation distance of photons by sampling an exponential distribution with parameter κ_f. We limit the photon generation to a maximum of 32 computational photons per cell per time step, which introduces some additional stochastic fluctuations in the ionization level ahead of the streamers.

2.3. Optical signature

For comparison with optical observations we calculate the number of excitations into the first positive system $N_2\left(B^3\Pi_g\right)$ of molecular nitrogen. We represent the accumulated optical emission density until time t as

$$n_{1PN2} = \frac{A_k}{A_k + k_q N} n_{N_2(B^3\Pi_g)}, \tag{8}$$

where the spontaneous emission rate is $A_k = 1.7 \times 10^5$ s^{-1} and the collisional quenching constant is $k_q = 8 \times 10^{-18}$ m^3 s^{-1} [19], which compensates for reduced optical emissions at lower altitudes. The relative radiative emission rate $\frac{A_k}{A_k + k_q N}$
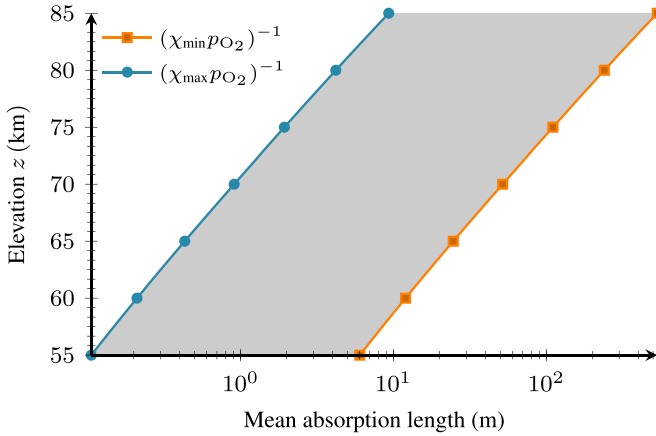
Figure 3. Minimum and maximum mean absorption lengths for ionizing photons at various altitudes. The mean absorption length of all ionizing photons in our model falls inside the shaded region.

from $N_2\left(B^3\Pi_g\right)$ varies from approximately 0.99 at $z = 80$ km to 0.8 at $z = 60$ km.

The effective lifetime of the $N_2\left(B^3\Pi_g\right)$ state is $A_k^{-1} \approx 6\,\mu$s, while typical time scales for the morphological evolution of sprites are $10^{-5} - 10^{-3}$ s. Excitation into and emission from the $N_2\left(B^3\Pi_g\right)$ state is thus virtually instantaneous on the sprite time scale. As with the accumulated emission, the instantaneous emission is represented as

$$S_{1PN2} = \frac{A_k}{A_k + k_q N} S_{N_2(B^3\Pi_g)}. \tag{9}$$

2.4. Initial data

We consider an initial electron density

$$n_e\left(z\right) = \frac{n_0}{2}\left[1 + \tanh\left(\frac{z - z_0}{L}\right)\right], \tag{10}$$

with $n_0 = 5 \times 10^9$ m^{-3}, $z_0 = 83$ km and $L = 1$ km, i.e. with negligible charge except in the ionosphere where $n_e \approx 5 \times 10^9$ m^{-3}. The initial ion densities are $n_{N_2^+} = 0.8 n_e$ and $n_{O_2^+} = 0.2 n_e$, respectively.

The thundercloud field is modeled as an initially electrically neutral cloud which transfers charge to the ground such that the space charge density in the thundercloud is

$$\rho_{tc}\left(t, \boldsymbol{x}\right) = -\rho_0 \exp\left[-\frac{1}{2}\left(\frac{|\boldsymbol{x} - \boldsymbol{x}_0|}{R}\right)^4\right]\left(1 - e^{-t/\tau}\right), \tag{11}$$

with $R = 10$ km, $\boldsymbol{x}_0$ set to 10 km above ground, $\tau = 0.1$ ms, and $\rho_0 = 6.4 \times 10^{-3}$ C km^{-1}. The total charge in the cloud is approximately -41 C.

No other sources of preionization [25] or preconstructed field distributions [26] were used in order to trigger any specific features of the sprite. Our model therefore permits the sprite to evolve naturally from only the ionospheric electrons and the electric field imposed by the charge distribution in the thundercloud.

2.5. Numerical discretization

All calculations in this paper were done using the chombo-discharge code [27], which we have used for numerous discharge simulations in the past [22, 27–32]. We solve the equations of motion over a 400 km $\times$ 400 km $\times$ 200 km region, using an adaptive Cartesian mesh. The base grid consists of $256 \times 256 \times 128$ cells, with another 11 levels of mesh refinement that are dynamically adapted throughout the simulation, i.e. the effective grid size is $524\,288 \times 524\,288 \times 262\,144$ cells and the finest representable grid resolution is approximately 0.76 m. Grid cells are refined if

$$\overline{\alpha}\Delta x \geqslant 1, \tag{12}$$

and coarsened if

$$\overline{\alpha}\Delta x \leqslant 0.2, \tag{13}$$

where $\overline{\alpha}$ is the effective Townsend ionization coefficient and Δx is the local grid resolution.

The temporal integration uses a Godunov splitting between plasma transport and reactions, where the transport equations are discretized in time using a Corner Transport Upwind (CTU) scheme with a monotonized central limiter [33] for the normal slopes. The Poisson equation is solved using a geometric multigrid method with V-cycling. We use a semi-implicit coupling between the Poisson equation and the transport equations (e.g. see [34]) in order to eliminate the dielectric relaxation time step constraint. Complete details regarding the discretization method are given in the chombo-discharge documentation [27]. The simulations in this paper used up to 25 600 CPU cores with mesh sizes up to 3×10^{-9} grid cells, and completed in about a day. Radiative transfer accounted for about 40% of a time step cost, which is due to sampling of approximately 20×10^{-9} computational photons per time step. Unfortunately, we were unable to load balance our way out this bottleneck as the remapping of photons to CPU ranks took place as an all-to-all process using a substantial amount of computational particles, which led to some load imbalance in the communication pattern for the discrete photons.

3. Results

Our results track a sprite from its birth in the halo after the lightning strike until $t \approx 11$ ms. The sprite initiated at approximately $z = 80$ km and extended downwards to approximately 63 km, at which point we terminated the computer simulation due to a decreasing reliability as the numerical resolution relative to the physical quantities of interest decreased. When we analyze the computer simulations we consider various quantifications such as three-dimensional isosurface reconstruction, planar slices, and images. The latter are defined by solving a simplified radiative transfer problem between the sprite emissions (n_{1PN2} and S_{1PN2}) and a reference plane that looks into the sprite from either the x or y direction. Alpha channels are then added to the instantaneous emission images, which are then overlaid the images of the long-exposure emissions. Figure 4 shows an image of the sprite emissions at $t = 10.72$ ms along
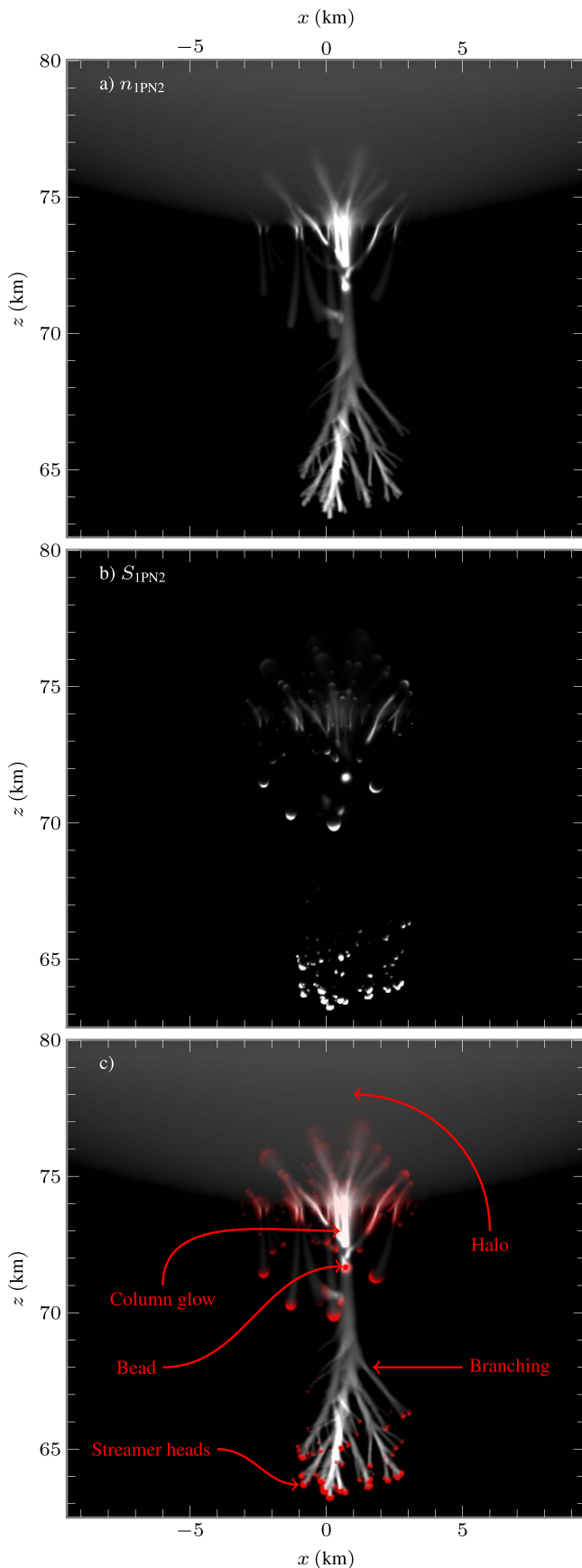
Figure 4. Images of the optical emissions from a sprite discharge simulation. (a) Accumulated emissions. (b) Instantaneous emission. (c) Overlaid emissions.
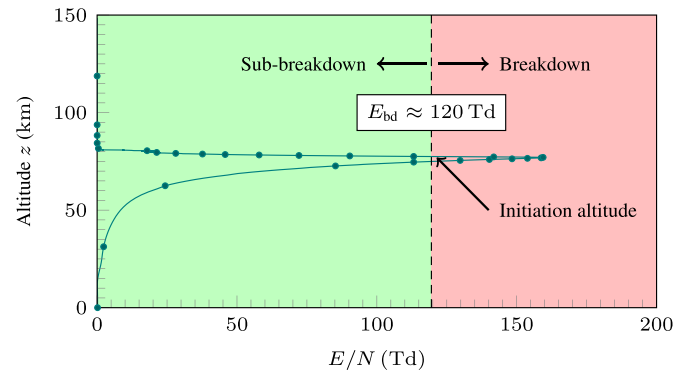

Figure 5. Reduced electric field above the thundercloud after the initial lightning strike ($t = 1.25$ ms).

with several indicated optical signatures, and is the simulation case that we systematically analyze.

3.1. Halo initiation

First, we discuss initiation of the halo. Charge transfer from cloud to ground results in a dipole field from the remaining positive thundercloud charge and ground, which drops off with altitude as z^{-1}. As the atmospheric density decays exponentially with altitude it results in a field $E/N > E_{br}$ at altitudes 75–83 km after $t \approx 0.15$ ms, which is where the halo initiates. Initiation does not extend into the ionosphere since the dielectric relaxation time is $\mathcal{O}\left(10^{-10}\text{ s}\right)$ in this region, and thus the electric field is negligible above altitudes of 83 km. Figure 5 shows how the reduced electric field has increased above the thunderstorm after the lightning strike, showing a thin layer of above-breakdown fields at altitudes of $z \approx 80$ km.

The time evolution of the halo emissions is given in figure 6, showing data-slices of n_{1PN2} and S_{1PN2} through the center of the halo. Optically, this will be observed as a large, luminous region that propagates downwards from the lower ionosphere, which is consistent with high-speed imaging observations [2] as well as several other theoretical studies [16].

We have not studied the initiation altitude of the sprite halo with other parameters, but observe that this is determined by (1) the charge moment (and temporal characteristic) of the lightning strike, and (2) the altitude of the ionospheric boundary. The ionosphere has no internal electric field on the timescale of sprites, so its lower boundary determines the upper cutoff of E/N as shown in figure 5. As N decays exponentially with altitude, the precise altitude of the ionospheric boundary is of some importance since deviations by just a few kilometers lead to large variations in the charge moment required for initiating the halo.

3.2. Halo breakup and streamer formation

Next, we present computational observations preceding halo breakup into streamer filaments. Experimental high-speed imaging [2] shows that downward propagating streamers initiate at bottom of the halo, either spontaneously or from brightening mesoscopic inhomogeneities. Figure 7 shows the
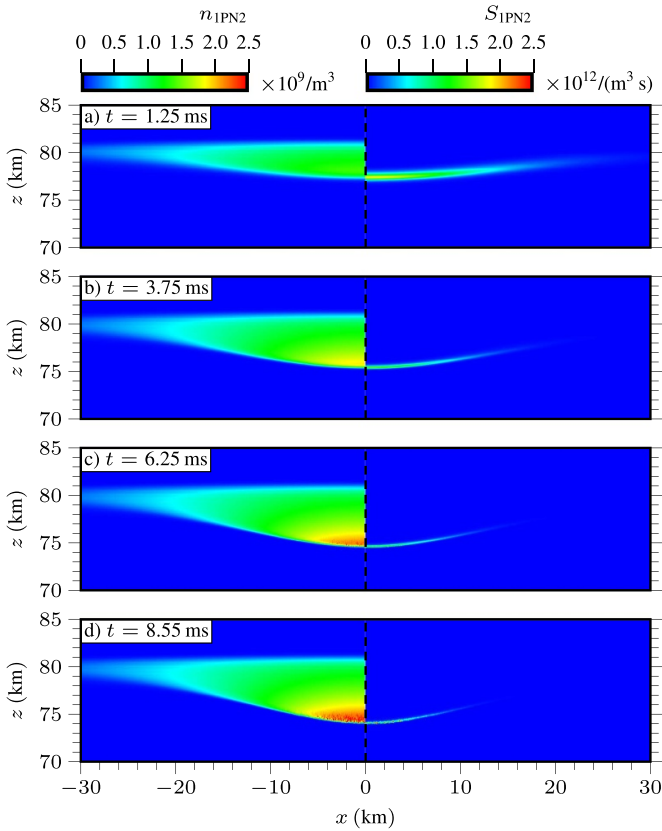
Figure 6. Cross-section of the simulation data showing the accumulated (n_{1PN2}) and instantaneous (S_{1PN2}) optical emissions. The data shows slices through mesh-based densities at the center of the sprite halo (i.e. they are not projections of emissions onto a camera aperture.) .

formation of such a streamer in the computer simulations, which here initiates at the bottom of the halo at $z \approx 74$ km after $t \approx 8$ ms. Initially, only a single columniform streamer emerges, whose optical signature is characterized by emission from the streamer head and a column glow in its tail. Other streamers emerge later from the halo, but are not yet discernible in figure 7. We also observe that streamer emergence from the halo is not instantaneous and there is a significant temporal delay between the stagnation of the halo and the emergence of the sprite. Figure 6 shows that the halo front reaches an altitude of $z \approx 75$ km after $t = 6.25$ ms, but the streamer emerges about two milliseconds later.

Various mechanisms have been suggested as explanations for the halo breakup, such as 'collapse' of the halo into a sprite streamer [16], or initiation through mesospheric disturbances such as gravity waves [35]. Here, a single streamer emerges spontaneously from the halo, which we attribute to stochastic fluctuations in the electron density below the halo edge. These fluctuations appear because as the halo descends downwards it also encounters an increasing air density, which approximately doubles every 5 km. The production of ionizing photons at the halo edge then decreases, as does the mean free path length of the photons. Photoionization in front of positive streamers is known to stabilize filaments [21, 22] in the sense that as photoionization is increased, electron density fluctuations in front
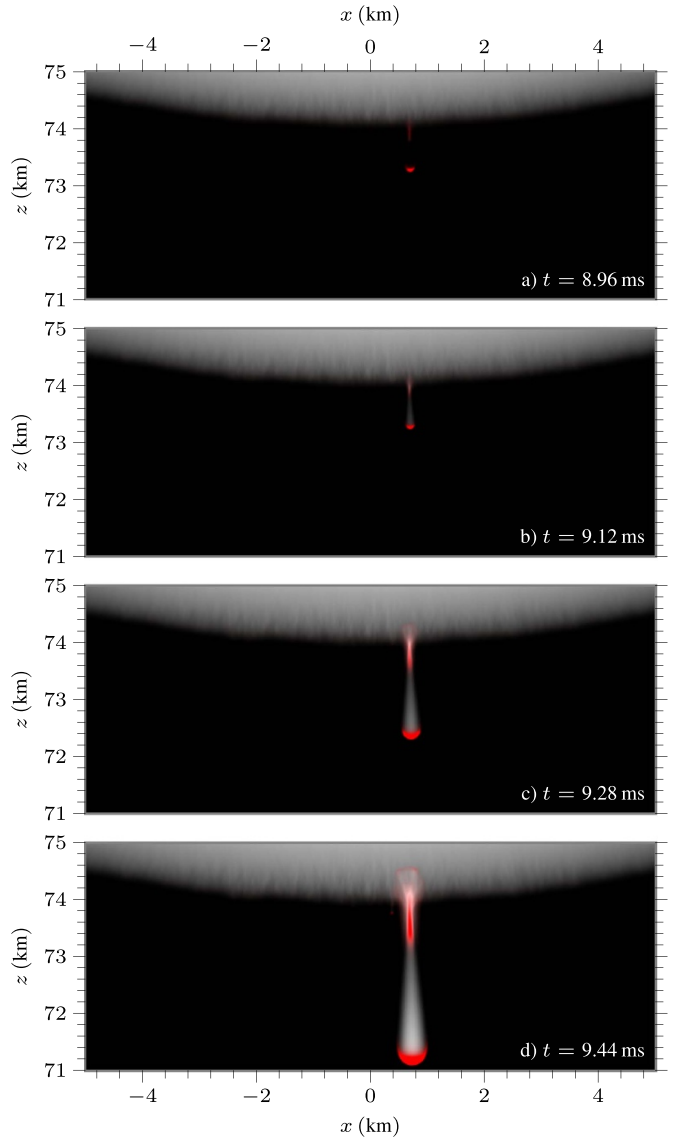

Figure 7. Accumulated and instantaneous optical emission images from n_{1PN2} during halo breakup. The emerging streamer emits light both from its tail and its downwards propagating head.

of the streamers decrease. These fluctuations would otherwise grow exponentially towards the streamer head (or halo edge, in this case). Correspondingly, as photoionization is reduced these density fluctuations become increasingly relevant.

Figure 8 shows the electron density and photoionization density near the halo edge, plotted together with a contour of $\alpha = \eta$ which shows the ionization zone. We observe, firstly, that the ionization zone is much longer (≈ 1.3 km) than the photon absorption length (1–100 m) and few photons (if any) reach the edge of the ionization zone. Substantial fluctuations in the electron density in the ionization zone therefore occur as most photons are absorbed very close to the halo front. A comparatively low number of photons travel further into the ionization zone.

The fluctuations imposed by photoionization are superimposed on top of the ionospheric electrons. However, figure 8(b) shows that the electron density ahead of the halo at $z = 73$ km
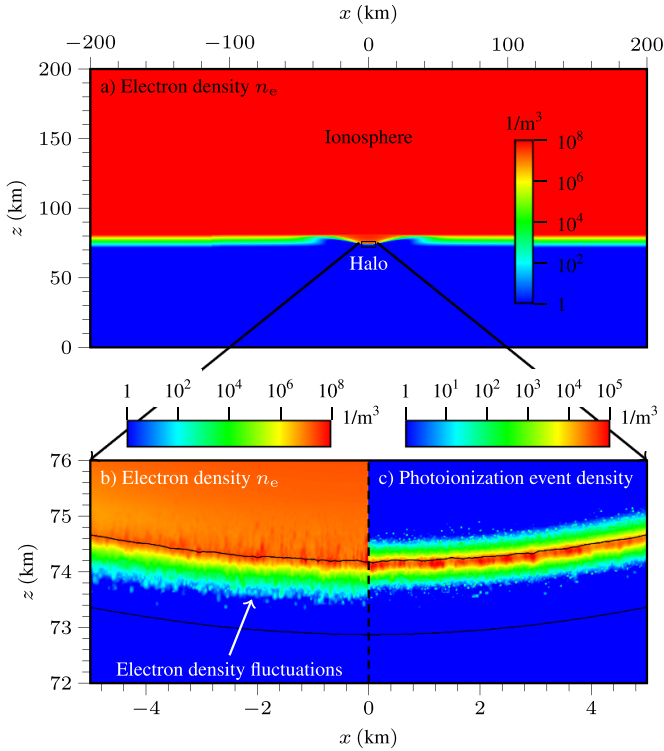
Figure 8. Electron density and photoionization distribution at the lower halo edge preceding halo breakup at $t = 8.57$ ms. The photoionization data shows the number of photoionization events per unit volume over an averaging time of approximately 1μs. The curved black lines in the lower two panels show contours $\alpha = \eta$.

Figure 9. Toy model for photon emission and absorption from a planar front of grid cells. Each cubic cell represents a numerical grid cell and isotropically emits N_γ physical photons.

represented as a planar front consisting of neighboring grid cells with spatial extents Δx, as indicated in figure 9. In this figure the location of each grid cell is $\boldsymbol{x}' = i\Delta x \hat{\boldsymbol{x}} + j\Delta x \hat{\boldsymbol{y}}$, and we assume that each grid cell isotropically emits N_γ photons. Note that the toy model coordinates are different from the sprite simulation coordinates. The average number of photons that are absorbed per unit volume at position $\boldsymbol{x}$ from the emission site $\boldsymbol{x}'$ is

$$I_\gamma\left(\boldsymbol{x},\boldsymbol{x}'\right) = \frac{\kappa N_\gamma}{4\pi \left|\boldsymbol{x} - \boldsymbol{x}'\right|^2} \exp\left(-\kappa \left|\boldsymbol{x} - \boldsymbol{x}'\right|\right), \qquad (14)$$

where κ^{-1} is the photon mean absorption length. Assuming an infinite planar front, and evaluating the expression at a distance z from the front yields

$$\begin{aligned} I_\gamma\left(z\right) = \sum_{i,j=-\infty}^{\infty} &\frac{\kappa N_\gamma}{4\pi \left|z^2 + \Delta x^2 \left(i^2 + j^2\right)\right|} \\ &\times \exp\left(-\kappa \sqrt{z^2 + \Delta x^2 \left(i^2 + j^2\right)}\right). \end{aligned} \qquad (15)$$

The number of physical photons generated per grid cell and time step in our simulations is typically $N_\gamma \sim 10^2 - 10^9$, depending on the location of the cell. Since the plasma density in the streamer decays with distance from the streamer head, the center of the halo streamer head emits many more photons than the front. The vertical length of the halo streamer head is also quite large, approximately 1 km, so the photons emitted from the center are absorbed quite rapidly, on average about 10 m from the emission site. Secondary electrons arising from these photons are therefore superimposed onto an already quite high plasma density, so these photons do not generate much preionization nor density fluctuations ahead of the halo. Fewer ionizing photons are emitted from the leading edge of the halo streamer head due to the much lower plasma density in those regions. An order-of-magnitude estimate from our simulations is $<10^3$ ionizing photons emitted per grid cell and time step. Unlike the photons that are emitted from the center of the streamer head, these photons escape the streamer

is $n_e \approx 10^{-8} - 10^{-6}$ m^{-3}, while equation (10) indicates a value of $n_e \approx 10$ m^{-3}. Similarly, following the electron density in figure 8(a) radially outwards from the center of the halo, e.g. on $z \approx 75$ km, we observe that the electron density has decreased to negligible levels on the sides of the halo. This decrease in electron density, both ahead of the halo as well as on its sides, occurs due dissociative attachment where free electrons are rapidly converted into negative ions during the halo descent. A more thorough discussion of dissociative attachment follows later in the paper, but we point out that at the halo initiation altitude this conversion occurs on the order of a few milliseconds (see figure 12), which implies that the number of free electrons ahead of the halo rapidly decreases after the lightning strike. The main implication is that the preionization ahead of the ionization zone of the halo is exponentially reduced in time, and correspondingly that the ambient ionospheric electrons ahead of the halo do not have a major impact on the magnitude of the photoionization-induced fluctuations.

The role of photoionization on the branching of positive and negative streamers have earlier been given by Liu and Pasko [19]. Here, we focus on the onset of discrete photon effects. One may derive an estimate for the distance at which the discrete nature of photons becomes non-negligible during a computational time step, using a simplistic model for the emission and absorption of ionizing photons. We consider a horizontal slice through the descending halo, which can be simplistically
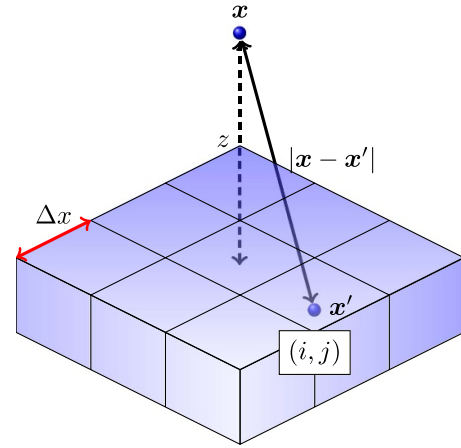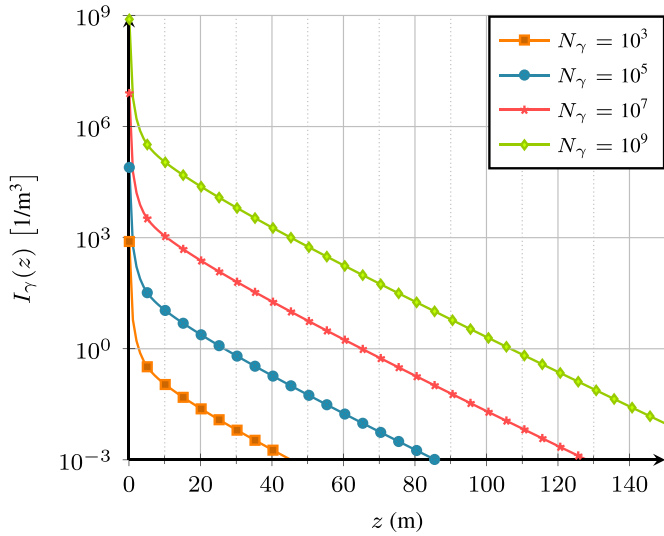
Figure 10. Radiative density as a function of distance z from a planar front, calculated using equation (15). Various numbers of initial photons N_γ are included, using an absorption coefficient $\kappa = \times 10^{-1}$ m^{-1}.

head and generate pre-ionization in regions where the plasma density is initially low. Thus, despite the fact that an overall large number of photons are emitted from the halo streamer head, a comparatively low number of photons are responsible for generating the electron density fluctuations at the halo front.

Figure 10 shows the average number of photons absorbed per unit volume at various distances from the planar front in figure 9, using equation (15). Let us consider a characteristic volume of 1 m^3 (one grid cell), where the curve with $N_\gamma \sim 10^9$ shows that single-photon effects manifest after $z \approx 110$ m, which is about a factor of ten shorter than the width of the ionization layer of the halo. For the curve with $N_\gamma \sim 10^3$, which is representative of the emissions from the leading edge of the halo, single-photon effects manifest after just $z \lesssim 5$ m. Thus, the discrete nature of photons manifests physically in the ionization zone of the halo. Correspondingly, and in analogy with past suggestions [19, 36], we conclude that the halo breakup is due to lack of sufficient photoionization for smoothing out plasma irregularities in the ionization zone, which ultimately trigger branching instabilities at the halo front.

Continuum models for photoionization [37, 38], which are quite popular in the streamer simulation community, leads to suppression of halo front fluctuations. Bagheri and Teunissen [21] and Marskar [22] have quite conclusively demonstrated that continuum models are unsuitable when describing branching instabilities for laboratory streamers, a conclusion which can now also be extended to sprites.

3.3. Column glow

Next, we evaluate the appearance of the glowing trail in the initial sprite streamer shown in figure 7. Originally, column glows for sprites were termed afterglows, and believed to occur due to delayed chemical reactions [39]. More recent computer
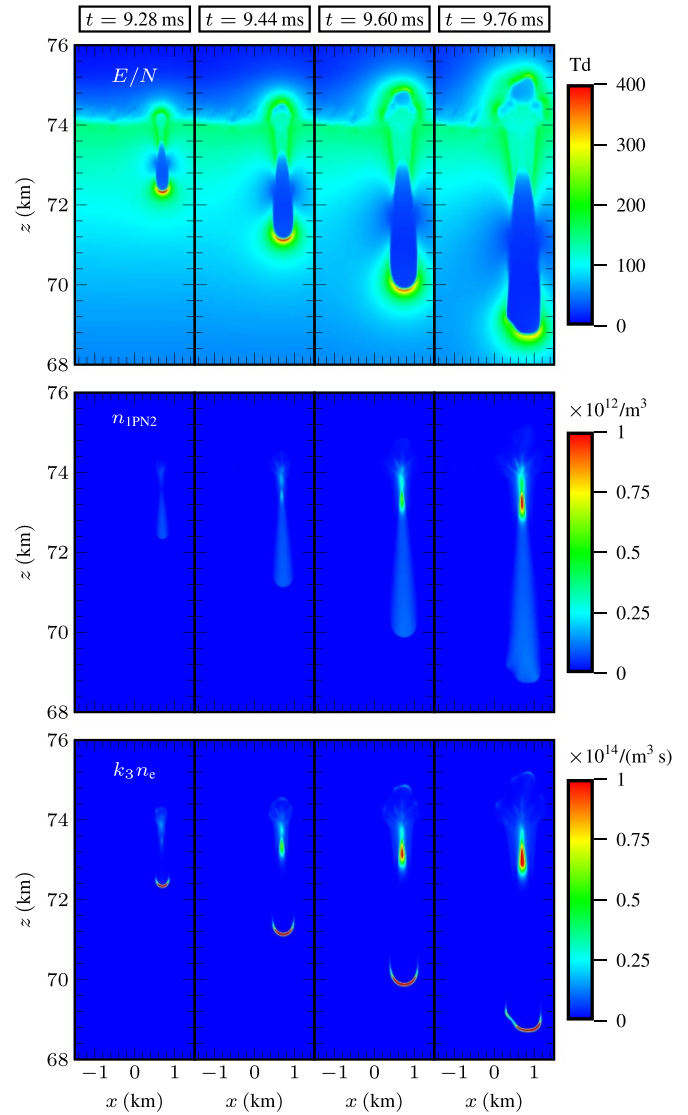

Figure 11. Snapshots of various simulation variables during glow formation (times are indicated above each column). Top row: Reduced electric field magnitude E/N. Middle row: Optical emission density n_{1PN2}. Bottom row: Dissociation term $k_3 n_e$.

simulations show that the emission is due to sustained excitation into the light-emitting 1PN2 state [40, 41].

Figure 11 shows the quantitative development of the initial column glow for the streamer, where the data is taken through a cross-section of the filament shown in figure 7. In the three rows we show the reduced electric field magnitude E/N, the accumulated emissions n_{1PN2}, and the dissociative attachment term $k_3 n_e$. We find that the glow develops just below the halo edge, and from a region where the electric field is initially quite high, approximately 90–120 Td. From the row containing n_{1PN2} we observe that the glow persists for a long time, and also extends downwards by about 100 m from $t = 9.28$ ms to $t = 9.76$ ms. The row containing $k_3 n_e$ shows that electron attachment in the glow region simultaneously increases during the same time window.

Luque *et al* [42] propose that the column glow is due to an attachment instability [43] in the streamer channel. While a
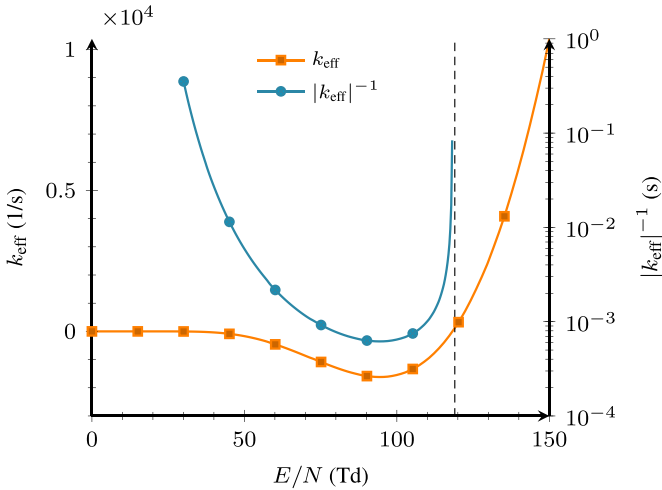
Figure 12. Effective ionization rate $k_{eff} = k_1 + k_2 - k_3$ at $z = 73$ km, plotted against the left axis. The other curve shows $|k_{eff}|^{-1}$ for the attachment region $E/N \lesssim 120$ Td and is plotted against the right axis.

detailed explanation can be found in [42], we consider a qualitative explanation of the phenomenon, which arises due to the nonlinearity of the impact ionization and attachment rates. Because dissociative attachment turns electrons into slower-moving ions, the net effect of the dissociative attachment reaction $e + O_2 \rightarrow O^- + O$ is a lowering of the conductivity of the streamer channel. If, at some short segment in the streamer channel the rate of dissociative attachment is locally higher, the conductivity of that segment will also decrease faster than elsewhere. Once the channel reaches a stationary or at the very least a quasi-stationary state, the electric field in that particular segment must correspondingly have increased due to charge conservation $\nabla \cdot \boldsymbol{J} = \nabla \cdot (\sigma \boldsymbol{E}) \approx 0$, where σ is the conductivity and $\boldsymbol{J}$ is the current density. Further evolution is then determined by the effective attachment rate, which is highly nonlinear in the electric field and is maximally effective around $E/N \approx 90$ Td. Figure 12 shows how the attachment rate $k_{eff} = k_1 + k_2 - k_3$ and the corresponding lifetime $|k_{eff}|^{-1}$ varies with E/N at 73 km altitude. Once attachment begins to reduce the conductivity and thus increase the electric field, the process reinforces itself as the attachment rate grows further, and the process is mostly effective around $E/N \approx 90$ Td. Incidentally, this value coincides with the initial electric field in the upper part of the sprite in figure 11 where the effective attachment rate is $|k_{eff}|^{-1} \approx 0.3$ ms, so dissociative attachment in this region is fully capable of substantially reducing the conductivity of the channel during the formation time of the sprite.

The computer simulations show that the glow extends slightly downwards with time, and also extends into a region where the initial electric field was not high enough to effectively feed the attachment process. For example, the rightmost column in figure 11 shows that the glow extends down to $z \approx 72.5$ km, but the initial field at this altitude (top left panel

in figure 11) was $E/N \approx 30$ Td, in which case the attachment lifetime is $\mathcal{O}(100 \text{ ms})$. This indicates that the column glow is not necessarily stationary, nor is there a hard cut-off into stable and unstable glow states as originally suggested by Luque *et al* [42]. On the other hand, our result suggest that the attachment process, conductivity reduction, and transition to a glow state is a continuous process that occurs everywhere in the channel at once. The process just happens to be particularly effective around $E/N \sim 90$ Td, and the corresponding decrease in conductivity rapidly leads to an increased electric field which then pushes the plasma towards a light-emitting state. The optical emission from the glow then occurs as usual: Excitation and emission from the first positive system of nitrogen.

According to figure 12, an initial electric field of E/N somewhere between 70–110 Td is probably required in order to efficiently feed the attachment instability at the millisecond time scale (at 73 km altitude). Typical fields in streamer channels are usually much lower, so transition to glow states do not occur at observational time scales in conventional, unperturbed streamer channels. For example, at around $E/N = 20$ Td, which is an often observed field in positive streamer channels, the effective attachment lifetime at 73 km altitude is about 40 s. Finally, since the curves in figure 11 scale with N, analogous phenomena probably exist for atmospheric pressure streamers. The mysterious pilot structures reported by Kochkin *et al* [44] could be indicative of an attachment-induced glow like we discuss above, but in this case it is not clear how the sufficiently high fields in the channel are initially reached. One may also conjecture that such structures are prone to increased local gas heating since, at least to a coarse approximation, the local heat input is given as $\boldsymbol{E} \cdot \boldsymbol{J}$ but only $\boldsymbol{J}$ is constant in stationary channels.

Questions have been raised regarding the role of electron detachment from O^- in the column glow. Kossyi *et al* [45] claim that detachment from O^- by collisions with ground states of O_2 and N_2 are negligible, and provide rates for collisions with ground state O_2 as well as excited molecules, specifically $N_2\left(A^3\Sigma_u^+\right)$, $N_2\left(B^3\Pi_g\right)$, $O_2\left(a^1\Delta_g\right)$, and $O_2\left(b^1\Sigma_g^+\right)$. The same rates are reproduced in Sentman *et al* [39]. If we consider, for the sake of simplicity since we do not solve for any of these excited states, that the density of $N_2\left(A^3\Sigma_u^+\right)$ is about the same as for N_2^+, the lifetime of the detachment reaction $O^- + N_2\left(A^3\Sigma_u^+\right) \rightarrow e + O + N_2$ at the observed glow altitude is approximately $\mathcal{O}(E3 \text{ s})$ when we use the rates given by Kossyi *et al* [45]. As this reaction is the fastest among the O^- detachment reactions provided by Kossyi *et al* [45], detachment due to collisions with the other excited states are also negligible. Likewise, Kossyi *et al* [45] provide a rate of $5E - 21$ m^{3}s^{-1} for the reaction $O^- + O_2 \rightarrow e + O_3$, but the time scale for electron detachment at sprite altitudes is then $\mathcal{O}(1 \text{ s})$, so none of these reactions appear to be relevant on the time scale of sprites. On the other hand, Luque *et al* [42] and Malagón-Romero *et al* [26] report that column glows disappear in the computer simulations when the electron detachment reaction $O^- + N_2 \rightarrow e + N_2O$ is included in the reaction set (N_2 indicates the ground state). The rate used
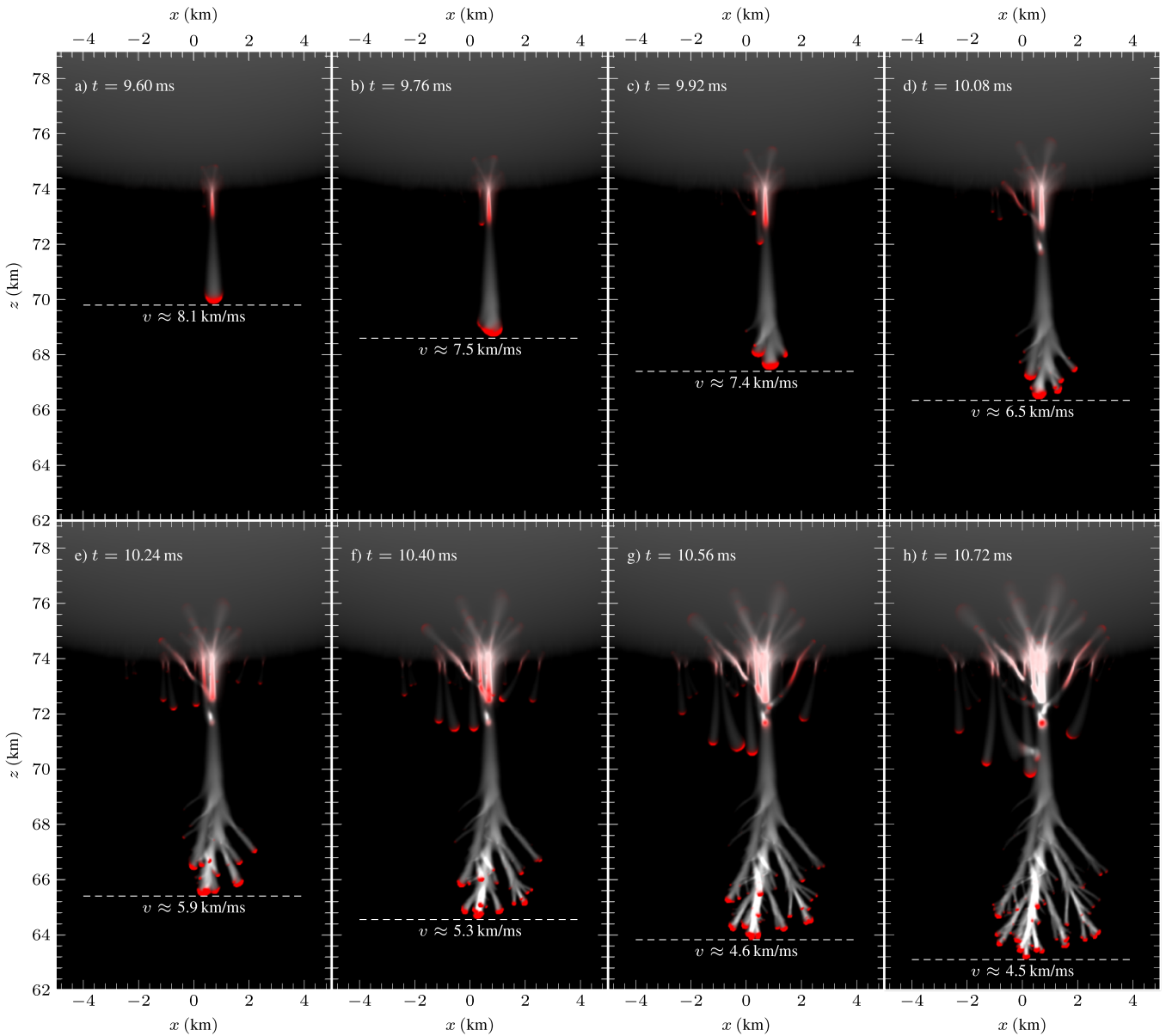
Figure 13. Long and short exposure images during the propagation phase. The dashed lines show the vertical streamer head position which were used to extract the indicated instantaneous velocities.

for this reaction traces back to experiments by Rayment and Moruzzi [46] who claim that ground states of N_2 participate in the reaction, which is at odds with claims by Kossyi *et al* [45]. Janalizadeh and Pasko [47] recently analyzed the experimental setup used by Rayment and Moruzzi [46] and propose that vibrationally excited N_2 polluted the experiments, and thus that the result is at least partially in error. Pending new experiments that clarify the roles of ground states and vibrationally excited states of N_2 in the detachment reaction $O^- + N_2 \rightarrow e + N_2O$, we have omitted this reaction from our chemistry set.

3.4. Downwards propagation and branching

Next, we analyze the propagation of the initial filaments after breakup from the halo and as they descend downwards. Figure 13 shows the accumulated and instantaneous optical

emissions until the various time instants indicated in each panel. The following features are observed:

(i) The initial streamer that originates in the halo breakup propagates down to approximately 68–70 km altitude before it branches.

(ii) As the streamer propagates downwards, excitation into the 1PN2 state in the tail of the initial streamer persists, which is optically observed as a glowing column at altitudes 72–74 km. These glows were analyzed section 3.3.

(iii) The sprite streamer velocity decreases with altitude, and is reduced from 8.1 $km\,ms^{-1}$ at 70 km altitude to 4.5 $km\,ms^{-1}$ at 63 km altitude.

(iv) Multiple streamer reconnections between individual filaments occur. These are particularly visible in figure 13(h) but occur as early as figure 13(c).

(v) A persistent, glowing bead region forms at $z \approx 72$ km, due to one of the streamer reconnections.

(vi) Negative streamers start from the top of the channels left behind by the downward streamers and propagate upwards into the halo.

Beads, reconnections, and upward streamers are analyzed in subsequent sections and we consider first the computational observations behind streamer branching. This is a fundamental property of streamers, and while no comprehensive theory for the phenomenon exists, the phenomenon is qualitatively understood. Physically, branching can only occur in the presence of local modification of the space charge layer around the streamer, e.g. through flattening or protrusions of some regions of it, or in the presence of density fluctuations, all of which can lead to additional local field maxima in the ionization zone. Such perturbations on the space charge layer can cause irregular growth of the plasma density ahead of the streamer, and thus act as nuclei for new branches. Curvature or density perturbations in the space charge layer is thus a necessary, but not sufficient, requirement for branching as other effects, e.g. electron diffusion or photoionization, may stabilize the front [48]. In laboratory experiments, streamers in air normally branch into two and occasionally three filaments [49], while imaging of sprites show that streamers may split into anywhere from 2 to about 10 filaments [50]. In gases with less photoionization, branching is more frequent [51].

In the computer simulation we observe in figure 13(a) through (c) that the sprite streamer radius increases as the streamer descends, and the ionizing photon absorption length simultaneously decreases. From figure 3 we find that at $z = 80$ km the mean absorption length of the photons is about 4–240 m, while at $z = 70$ km the corresponding lengths are 1–50 m. When the first streamer breaks out of the halo at $z \approx 74$ km its optical radius is approximately 250 m, while the maximum mean absorption length for photons is 200 m. As the streamer descends to 70 km its radius increases to 1 km, while the maximum mean absorption length simultaneously decreases to 50 m. Figure 14 shows a cross section of the electron density on the streamer axis, and demonstrates how these effects affect the streamer. In figure 14(a), some photoelectrons appear outside the ionization volume ahead of the streamer, while figure 14(b) through (d) show that the number of photoionization events outside the ionization volume gradually decreases with altitude.

A few qualitative evaluations of the underlying processes can now be made in the context of both laboratory and sprite streamers. Firstly, sprites generate more ionizing photons per electron impact ionization event than corresponding laboratory streamers since collisional quenching is negligible at sprite altitudes but not at ground pressure. For laboratory streamers, the amount of photoionization has been shown to substantially influence the amount of branching [21, 22, 52]. However, as discussed in section 3.2 the distribution of the ionizing photons also matters, and the sprite streamers observed in the computer simulations have large radii compared to the photon absorption length. As the volume of the ionization zone ahead of the streamer also increases with streamer radius, most of the
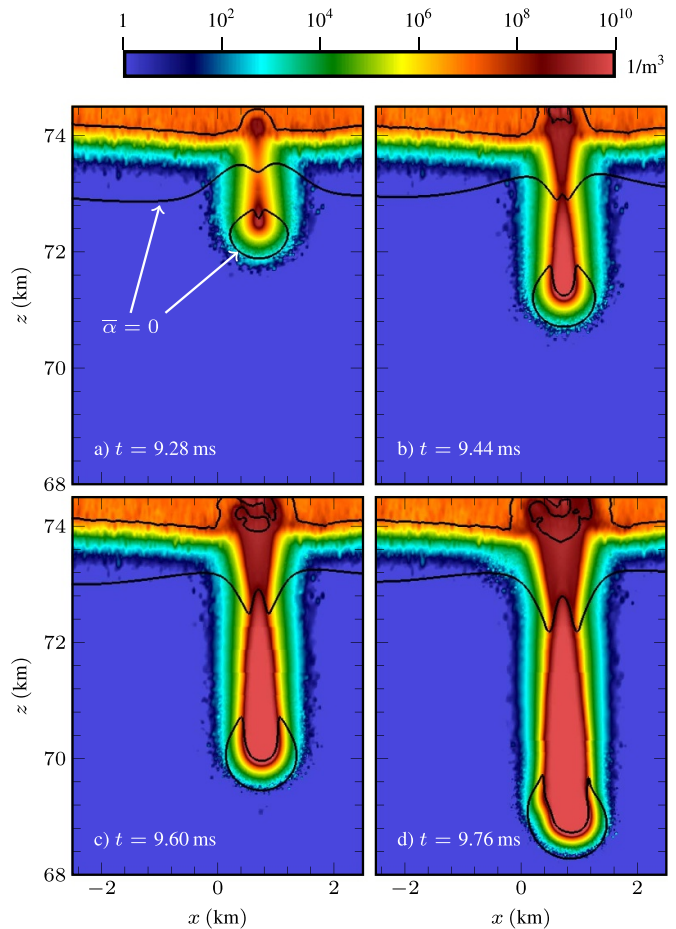

Figure 14. Time series of the electron density for the initial sprite streamer. The solid lines indicate the contour $\alpha = \eta$.

emitted photons in a sprite streamer are, relatively speaking, absorbed close to the streamer head. As with the sprite halo, the radiative intensity drops off exponentially with distance from the streamer head, e.g. with a characteristic length scale of approximately 25 m at $z = 70$ km, so far fewer photons reach the outer edges of the ionization zone. Although more electron-ion pairs from photoionization are generated closer to the streamer head, the ones that are generated further out appear in regions where the electron density is already low, and they multiply exponentially over a longer distance than the ones starting closer to the streamer head. For positive streamers these electron-ion pairs can thus exacerbate fluctuations in the front. Incidentally, we believe this is also one of the reasons why small-diameter laboratory streamers branch less frequently than large-diameter ones [53], as the ionization zone for small-diameter streamers is then also smaller and discrete photon effects primarily manifest outside of it. In summary, we propose that branching for sprite streamers occurs in precise analogy with laboratory streamers in air, i.e. due to growth of a Laplacian instability at the front of the streamer.

3.5. Sprite beads

Sprite beads are luminous spots that appear in sprite streamer channels, and whose time scales indicate that they are not
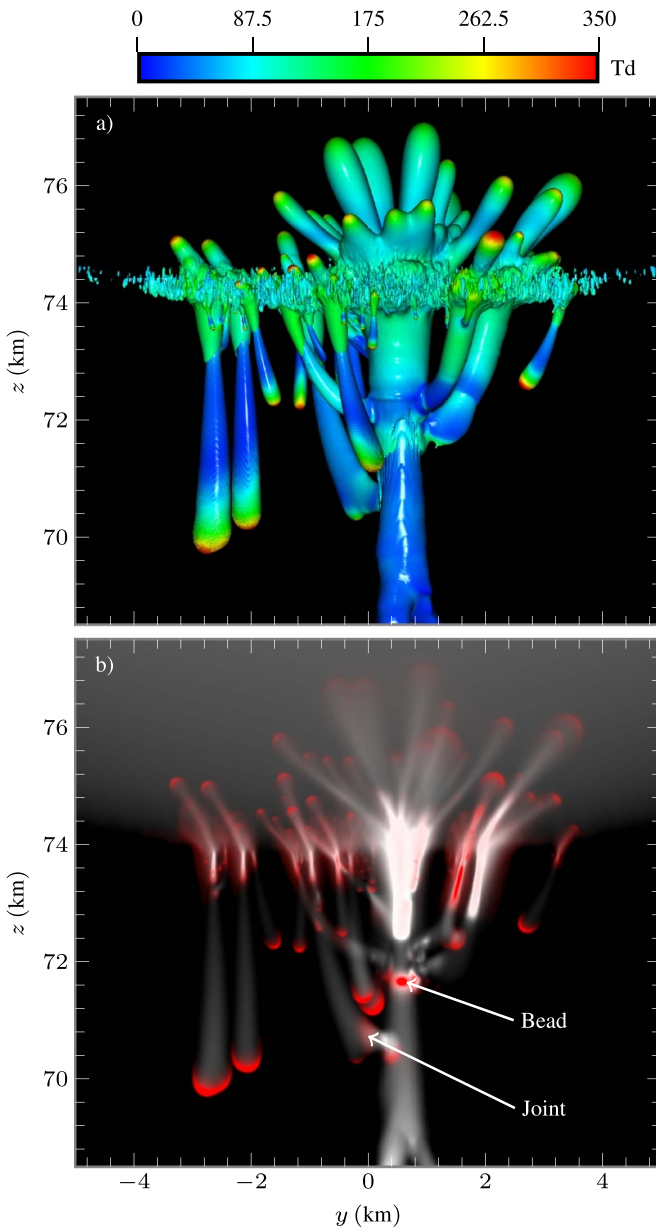
Figure 15. (a) Isosurface plot of $n_{1PN2} = 5 \times 10^9$ m^{-3}. Colors indicate values of the reduced electric field E/N. (b) Image of accumulated and instantaneous sprite bead emissions. White colors indicate accumulated emission intensities and red colors indicate instantaneous emissions.

Figure 16. Two-dimensional slice through the streamer bead region at $t = 10.72$ ms. (a) Instantaneous emissions from 1PN2. (b) Reduced electric field. (c) Electron density. (d) Electron impact terms, i.e. $\overline{\alpha}n_e$.

slowly moving or stagnant streamer heads. These structures are consistently captured in high-speed imaging experiments [2, 3], and are both stationary and long-lasting. Cummer *et al* [2] report on bead formation due to streamer reconnection, i.e. collisions between streamer channels, and suggest that a number of beads appear from this process. Other types of beads appear to form spontaneously, or at the very least without a clear observation of a streamer reconnection, and the mechanism leading to formation of these types beads is currently not known. Luque *et al* [42] propose that bead emissions are due to the same process as glows, i.e. due to an attachment instability in the streamer channel.
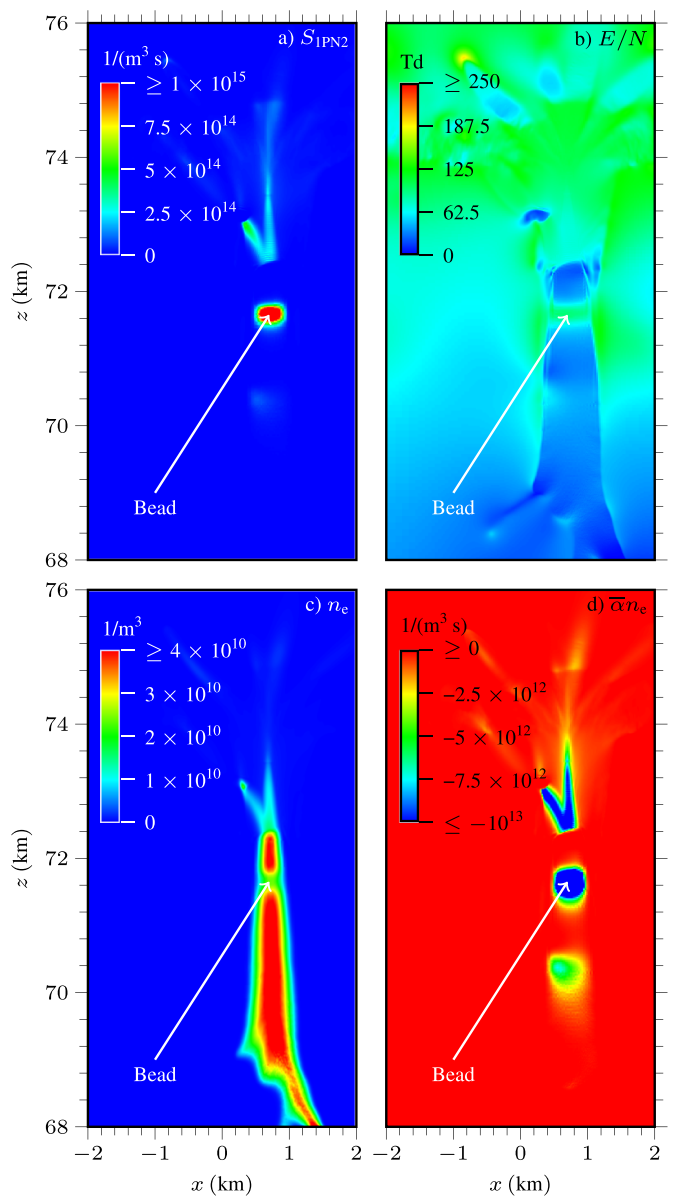
In the computer simulation we observed numerous streamer reconnections, all of which occurred between downward propagating streamers. Figure 15(a) shows an isosurface plot of the 1PN2 emissions (colors indicate electric fields), where several reconnections can be observed. Note that the reconnections are due to late-emerging positive streamers propagating downwards from the halo edge and connecting to the tail of early streamers, and not upward shooting negative streamers. Additional reconnections also occurred, but are hidden behind some of the isosurfaces shown in the plot. Figure 15(b) shows a corresponding image of the accumulated and instantaneous optical emissions, where a bead has formed at $z \approx 71.5$ km.

To explain the emissive properties of the beads, figure 16 shows a 2D slice of the simulation data through the streamer

channel containing the bead indicated in figure 15. In figure 16(a) through (c) we include the instantaneous emissions from 1PN2, the reduced electric field, and the electron density. Figure 16(d) also shows the attachment region of the electron impact term, i.e. the negative region of $\overline{\alpha}n_e$. In the bead we observe the following features:

1) A localized spot of persistent 1PN2 excitations.
2) A localized and comparatively high electric field $E/N \approx$ 90 Td.
3) A locally decreased electron density, and thus also a locally decreased conductivity.
4) An increased rate of dissociative attachment $e + O_2 \rightarrow O^- + O$.

These features are the hallmark features of the attachment instability that we discussed in section 3.3 and we thus arrive at the same conclusion as Luque *et al* [42]: Beads are due to persistent excitation of the first positive system, fed by an attachment instability that locally increases the electric field and thus enhances optical emissions.

In the computer simulations, not all reconnections resulted in bead formation and the beads were often, but not always, centered on the streamer channels. In figure 15 we have marked a section by 'Joint', and we have observed that these structures also cause persistent light emission, although the glow from these regions is much weaker than beads centered on the channel. Additional manifestations of these glow features are available in figure 18 at the end of this paper. Investigations of the electric field in these regions again display the typical signature of an attachment instability, and we thus conjecture that most (perhaps all) beads and long-lasting glowing structures are manifestations of the attachment instability. However, bead formation only occurs at observational time scales if streamer channels are sufficiently perturbed by electric fields reaching approximately 70–110 Td in the channel, as this is the only range of electric fields where the attachment instability can be fed sufficiently fast. Since the field is the primary trigger of the attachment instability, the evolution of sprite beads is quite subtle and there are probably several mechanisms that leads to their formation. Our calculations show that beads occasionally appear in association with streamer reconnection, while spontaneous beads were not observed. This is not to suggest that spontaneous bead emergence does not occur at all, but the conditions for it to happen were either not present in our computer simulations, or the simulation was not run long enough for these beads to appear. In at least one case did we observe structures that could be interpreted as a spontaneous bead at lower altitudes ($z \approx 69$ km in figure 18), but where closer examination of the data shows multiple streamer reconnections just above the bead region.

3.6. Sprite reconnection

For both sprite and laboratory streamers, various mechanisms for streamer reconnection [2, 54] have been proposed. Luque *et al* [55] propose that under very specific circumstances merging can occur due to overlapping photoionization regions. For this to happen, the streamers need to be separated by a
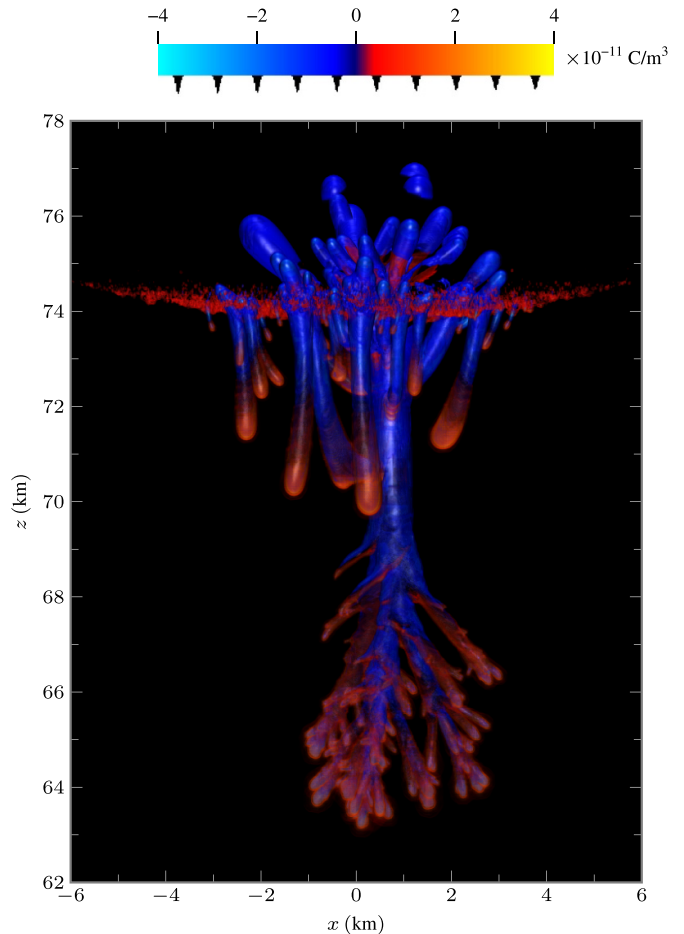

Figure 17. Space charge distribution ρ in the sprite. Warm colors indicate positive space charge and cold colors indicate negative space charge, which can be mapped to the indicated color and opacities. The figure uses a truncated color range with semi-transparent layers so that the charge in both the core and space charge layers can be visualized. The curves at the bottom of the colorbar indicates which charge densities are visible.

distance shorter than the photon mean free path length, and the ionization volumes ahead of the streamers must also overlap. However, in our computer simulation the streamers initiate quite far from each other, up to 3 km, and still manage to reconnect, so merging of photoionization volumes cannot be the explanation in our simulations. This type of reconnection has not been observed in other 3D computer simulations of laboratory streamers [22, 56] either. As magnetic attraction is not represented in our computer simulations, and the late streamers bend into the main channel even though they are initially widely separated, the phenomenon must be purely electrostatic. Cummer *et al* [2] conjecture that this proceeds due to one streamer branching inducing a charge on the other, but as we will see, our calculations do not support this explanation either. Rather, as first demonstrated by Luque and Ebert [40], we find that negative charge accumulates on the tail of the streamers, which then attracts the positively charged heads of the late-emerging streamers. The data corroborating this mechanism is given in figure 17, which shows the space charge distribution of the sprites. In the descending streamer heads the

space charge distribution is reminiscent of laboratory streamers in the sense that they are slightly negatively charged in their core but have positively charged space charge layers. However, both the core and outer layer of the tails of the sprite streamers are negatively charged, which is what causes the attraction between the early and late emerging streamers.

3.7. Upwards propagation

Figure 13 shows that several negative streamers also propagate upwards into the halo region. All of the upward streamers that are visible in the figure start from the top of the channels left behind by downwards streamers, although some of these visually can appear as if they started from the bottom of the glow. For example, the streamers on the right hand side of figure 15(b) started as downwards streamers that connected to the main channel and then later transitioned into upwards streamers.

From figures 13, 15 and 17 we extract the following qualitative information:

(1) The upward streamers are characterized by negative charge in their heads and are thus negative streamers.
(2) The upward streamers are characterized by a lower electric field at their tips than the downwards propagating positive streamers. Depending on their radius, we find fields roughly in the range 150–350 Td, while for the downwards positive streamers the fields are typically 250–450 Td.
(3) There is a slight delay between the downward streamer initiation and the upward streamers. From figure 7 we observe that by the time the negative streamers initiate, the downward streamer has already propagated a few kilometers.
(4) The luminosity of the upward streamers is comparatively low, and essentially merge with that of the halo.

As the upward streamers that appear in the computer simulations have low luminosity, we characterize our computer simulation as a column sprite rather than a carrot sprite, as the latter have very large luminous tops that can be easily identified [3]. High-speed imaging of sprites show that upward streamers can be launched from the bottom of the column glow, which was recently demonstrated by Malagón-Romero *et al* [26]. This type of upwards propagation was not observed in our computer simulations. However, returning to figure 16(b) which shows the reduced electric field through a cross section of the streamer containing the bead, the electric field on the sides of the channel lies in the range 90–120 Td, which is just below the breakdown field. These fields are found both around the bead region and the lower edge of the column glow, but clearly the fields were not sufficiently high for launching negative streamers. Nonetheless, our simulations lends credence to the fundamental mechanism suggested by Malagón-Romero *et al* [26], as we here self-consistently show that comparatively high fields develop on the sides of the streamer channel in column glow and bead regions.

4. Summary

4.1. Conclusions

We have presented a theoretical examination of the birth and evolution of a column sprite in the Earth atmosphere, using self-consistent models and realistic atmospheric conditions. The computer simulations allowed us to identify physical processes associated with commonly observed optical signatures. We interpret the results as follows:

- Halo breakup occurs due to an instability at the halo edge, triggered by electron density fluctuations in front of the halo. These fluctuations originate due to absence of sufficient photoionization-enabled smoothing in the relatively long ionization zone of the halo as it descends into increasingly dense air.
- Sprite streamer branching occurs in analogy with both halo breakup; growing fluctuations at the streamer edge occur due to a lack of sufficient photoionization in the ionization zone of the streamers, which triggers branching.
- The formation of a column-shaped glow region, which for the record is not a stationary structure, is attributed to the creation of a low-conductivity and high-field region within the streamer channels. This process is self-enhancing as the rate of dissociative attachment increases with the electric field magnitude up to $E/N \sim 90$ Td, where the process is particularly fast and effective. In principle, this gradual transition towards a light-emitting state occurs everywhere in the streamer channels, but the process is primarily effective for $E/N \in [70\,\mathrm{Td}, 110\,\mathrm{Td}]$. The electric field in unperturbed channels is much lower than this, and such channels do not develop glows.
- Optical emission from sprite beads, which have long perplexed researchers, also occur due to an attachment instability that is triggered by sprite streamer reconnection, in agreement with past suggestions [2, 42].
- Streamer reconnection occurs due to electrostatic attraction between the positively charged heads of late emerging streamers and the negatively charged tails of early emerging streamers.

4.2. Outlook

In this paper we systematically analyzed a single sprite simulation, but remark that the above features emerged also in other computer simulations. Like real sprites, there is great variability in the sprite morphology also in the computer simulations. For example, although we selected a computer simulation in which a comparatively few number of branches emerged and only a single sprite bead was conclusively observed, other simulations displayed emergence of several beads. Figure 18 shows the accumulated optical emissions in a different computer simulation using precisely the same physical and numerical parameters, in which case additional beads can be identified. These beads also developed due to the attachment instability, and the difference in number of beads is primarily related to the stochastic morphology of the sprite.
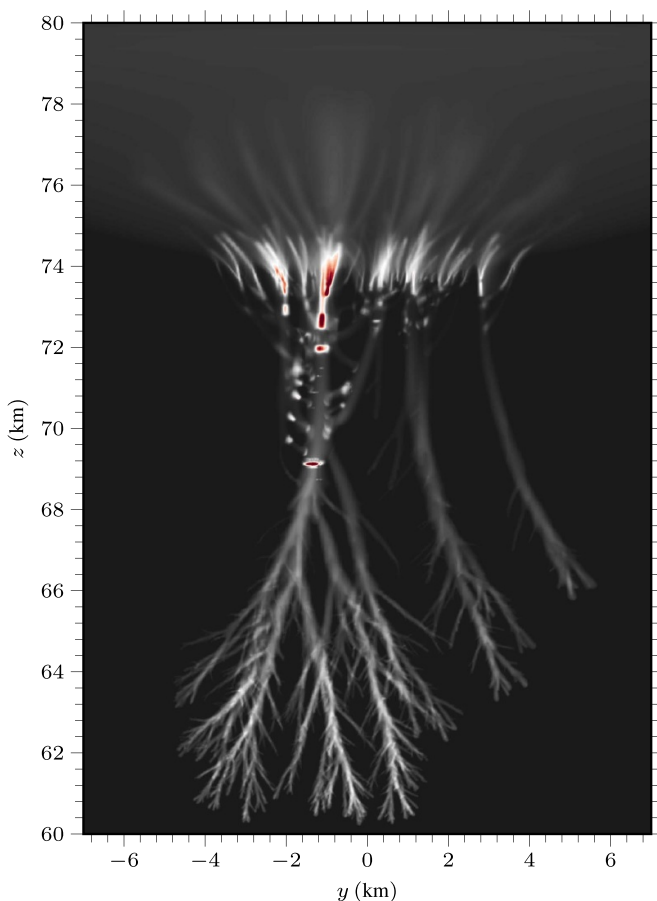
Figure 18. Example image of another computer simulation exposing a different sprite morphology in which multiple beads emerged, but sharing fundamental physical features with the in-depth analyzed sprite simulation. Note that the figure shows the accumulated sprite emissions but uses a different color map than preceding images.

Our computer simulation(s) also explore a relatively narrow parameter space, as we do not explore different lightning strike characteristics nor atmospheric disturbances such as gravity waves [35], both of which are known to strongly influence the initiation and propagation of sprites. Another issue is that precise ionospheric conditions are required in order to model specific sprites. In this study we used a simplistic model for the ionosphere with a sharp decay below $z \approx 83$ km, i.e. $L = 1$ km in equation (10). Recent calculations [57, 58] suggest that the electron density below this altitude could be higher than in our calculations. However, as we discussed in section 3.2 the free electrons are quite efficiently converted to negative ions ahead of the halo, and the level of preionization does not affect our conclusions regarding the basic formation mechanisms or optical structures. More specific ionospheric conditions can nonetheless affect the initiation altitude of the sprite, as well as the thundercloud charge required for initiation.

4.3. Impact

Our results hold dual significance: First, we identify physical mechanisms associated with optical signatures, explaining

previous high-speed imaging observations [2, 3]. It is also clear that many sprite phenomena are linked and cannot be understood in isolation. For example, sprite reconnection occurs due to attraction between the negatively charged tail of a sprite and the positively charged head of another sprite, and the ensuing collision can then occasionally lead to appearance of sprite beads. Second, we demonstrate the feasibility of performing comprehensive 3D simulations of sprites. While this step required use of high-performance computing, these capabilities are crucial for quantifying the physical mechanisms of sprites, including the production of chemical species and their long-term impact on the Earth atmosphere. Theoretical investigations of the type that is presented here are probably a key factor in achieving a complete quantitative understanding of sprites both on Earth and in other planetary atmospheres.

Data availability statement

Acknowledgments

ORCID iD

R Marskar ⓘ https://orcid.org/0000-0003-1706-9736

References

[1] Franz R C, Nemzek R J and Winckler J R 1990 Television image of a large upward electrical discharge above a thunderstorm system *Science* **249** 48–51
[2] Cummer S A, Jaugey N, Li J, Lyons W A, Nelson T E and Gerken E A 2006 Submillisecond imaging of sprite development and structure *Geophys. Res. Lett.* **33** L04104
[3] Stenbaek-Nielsen H C and McHarg M G 2008 High time-resolution sprite imaging: observations and implications *J. Phys. D: Appl. Phys.* **41** 1
[4] Kosar B, Yue J, Gerland O, Bor J, Simmons S and Lense R 2022 Spritacular—a citizen science project to study electrical discharges above thunderstorms *AGU Fall Meeting*
[5] Wilson C T 1924 The electric field of a thundercloud and some of its effects *Proc. Phys. Soc. London* **37** 32D

[6] Nijdam S, Teunissen J and Ebert U 2020 The physics of streamer discharge phenomena *Plasma Sources Sci. Technol.* **29** 103001

[7] Stanley M, Krehbiel P, Brook M, Moore C, Rison W and Abrahams B 1999 High speed video of initial sprite development *Geophys. Res. Lett.* **26** 3201–4

[8] Wescott E M, Stenbaek-Nielsen H C, Sentman D D, Heavner M J, Moudry D R and Sabbas F T S 2001 Triangulation of sprites, associated halos and their possible relation to causative lightning and micrometeors *J. Geophys. Res.* **106** 10467–77

[9] Barrington-Leigh C P, Inan U S and Stanley M 2001 Identification of sprites and elves with intensified video and broadband array photometry *J. Geophys. Res.* **106** 1741–50

[10] Miyasato R, Taylor M J, Fukunishi H and Stenbaek-Nielsen H C 2002 Statistical characteristics of sprite halo events using coincident photometric and imaging data *Geophys. Res. Lett.* **29** 29-1–4

[11] Newsome R T and Inan U S 2010 Free-running ground-based photometric array imaging of transient luminous events *J. Geophys. Res.* **115** A00E41

[12] Williams E, Downes E, Boldi R, Lyons W and Heckman S 2007 Polarity asymmetry of sprite-producing lightning: a paradox? *Radio Sci.* **42** RS2S17

[13] Gerken E A, Inan U S and Barrington-Leigh C P 2000 Telescopic imaging of sprites *Geophys. Res. Lett.* **27** 2637–40

[14] Marshall R A and Inan U S 2005 High-speed telescopic imaging of sprites *Geophys. Res. Lett.* **32** L05804

[15] Marshall R A and Inan U S 2006 High-speed measurements of small-scale features in sprites: sizes and lifetimes *Radio Sci.* **41** RS6S43

[16] Luque A and Ebert U 2009 Emergence of sprite streamers from screening-ionization waves in the lower ionosphere *Nat. Geosci.* **2** 757–60

[17] Hagelaar G J and Pitchford L C 2005 Solving the Boltzmann equation to obtain electron transport coefficients and rate coefficients for fluid models *Plasma Sources Sci. Technol.* **14** 12

[18] S. database 2022 *SIGLO database* (available at: www.lxcat.net) (Accessed 1 November 2022)

[19] Liu N and Pasko V P 2004 Effects of photoionization on propagation and branching of positive and negative streamers in sprites *J. Geophys. Res.* **109** A04301

[20] Pancheshnyi S, Nudnova M and Starikovskii A 2005 Development of a cathode-directed streamer discharge in air at different pressures: experiment and comparison with direct numerical simulation *Phys. Rev.* E **71** 1

[21] Bagheri B and Teunissen J 2019 The effect of the stochasticity of photoionization on 3D streamer simulations *Plasma Sources Sci. Technol.* **28** 1

[22] Marskar R 2020 3D fluid modeling of positive streamer discharges in air with stochastic photoionization *Plasma Sources Sci. Technol.* **29** 055007

[23] Stephens J, Abide M, Fierro A and Neuber A 2018 Practical considerations for modeling streamer discharges in air with radiation transport *Plasma Sources Sci. Technol.* **27** 075007

[24] Pancheshnyi S 2015 Photoionization produced by low-current discharges in O_2, air, N_2 and CO_2 *Plasma Sources Sci. Technol.* **24** 015023

[25] Köhn C, Chanrion O and Neubert T 2019 The sensitivity of sprite streamer inception on the initial electron-ion patch *J. Geophys. Res.* **124** 3083–99

[26] Malagón-Romero A, Teunissen J, Stenbaek-Nielsen H C, McHarg M G, Ebert U and Luque A 2020 On the emergence mechanism of Carrot sprites *Geophys. Res. Lett.* **47** e2019GL085776

[27] Marskar R and Meyer H K H 2023 A kinetic Monte Carlo study of positive streamer interaction with complex dielectric surfaces *Plasma Sources Sci. Technol.* **32** 1

[28] Marskar R 2019 An adaptive Cartesian embedded boundary approach for fluid simulations of two- and three-dimensional low temperature plasma filaments in complex geometries *J. Comput. Phys.* **388** 31

[29] Marskar R 2019 An adaptive Cartesian embedded boundary approach for fluid simulations of two- and three-dimensional low temperature plasma filaments in complex geometries *J. Comput. Phys.* **388** 31

[30] Meyer H K, Mauseth F, Marskar R, Pedersen A and Blaszczyk A 2019 Streamer and surface charge dynamics in non-uniform air gaps with a dielectric barrier *IEEE Trans. Dielectr. Electr. Insul.* **26** 9

[31] Meyer H K H, Marskar R, Gjemdal H and Mauseth F 2020 Streamer propagation along a profiled dielectric surface *Plasma Sources Sci. Technol.* **29** 1

[32] Meyer H K H, Marskar R and Mauseth F 2022 Evolution of positive streamers in air over non-planar dielectrics: experiments and simulations *Plasma Sources Sci. Technol.* **31** 1

[33] Colella P 1990 Multidimensional upwind methods for hyperbolic conservation laws *J. Comput. Phys.* **87** 171–200

[34] Ventzek P L G, Hoekstra R J and Kushner M 1994 Two-dimensional modeling of high plasma density inductively coupled sources for materials processing *J. Vac. Sci. Technol.* B **12** 1

[35] Liu N, Dwyer J R, Stenbaek-Nielsen H C and McHarg M G 2015 Sprite streamer initiation from natural mesospheric structures *Nat. Commun.* **6** 1

[36] Kulikovsky A A 2000 Role of photoionization in positive streamer dynamics *J. Phys. D: Appl. Phys.* **33** 11

[37] Bourdon A, Pasko V P, Liu N Y, Célestin S, Ségur P and Marode E 2007 Efficient models for photoionization produced by non-thermal gas discharges in air based on radiative transfer and the Helmholtz equations *Plasma Sources Sci. Technol.* **16** 23

[38] Luque A, Ebert U, Montijn C and Hundsdorfer W 2007 Photoionization in negative streamers: fast computations and two propagation modes *Appl. Phys. Lett.* **90** 081501

[39] Sentman D D, Stenbaek-Neilsen H C, McHarg M G and Morrill J S 2008 Plasma chemistry of sprite streamers *J. Geophys. Res.* **113** D11112

[40] Luque A and Ebert U 2010 Sprites in varying air density: charge conservation, glowing negative trails and changing velocity *Geophys. Res. Lett.* **37** 1

[41] Liu N 2010 Model of sprite luminous trail caused by increasing streamer current *Geophys. Res. Lett.* **37** L04102

[42] Luque A, Stenbaek-Nielsen H C, McHarg M G and Haaland R K 2016 Sprite beads and glows arising from the attachment instability in streamer channels *J. Geophys. Res.* **121** 19

[43] Douglas-Hamilton D H and Mani S A 1973 An electron attachment plasma instability *Appl. Phys. Lett.* **23** 508–10

[44] Kochkin P, Lehtinen N, Deursen A P V and Østgaard N 2016 Pilot system development in metre-scale laboratory discharge *J. Phys. D: Appl. Phys.* **49** 425203

[45] Kossyi I A, Kostinsky A Y, Matveyev A A and Silakov V P 1992 Kinetic scheme of the non-equilibrium discharge in nitrogen-oxygen mixtures *Plasma Sources Sci. Technol.* **1** 14

[46] Rayment S W and Moruzzi J L 1978 Electron detachment studies between O- ions and nitrogen *Int. J. Mass Spectrom. Ion Phys.* **26** 321–6

[47] Janalizadeh R and Pasko V P 2021 Implications of electron detachment in associative collisions of atomic oxygen anion with molecular nitrogen for modeling of transient luminous events *Geophys. Res. Lett.* **48** e2020GL091134

[48] Arrayás M, Ebert U and Hundsdorfer W 2002 Spontaneous branching of anode-directed streamers between planar electrodes *Phys. Rev. Lett.* **88** 4

[49] Heijmans L C, Nijdam S, Veldhuizen E M V and Ebert U 2013 Streamers in air splitting into three branches *Europhys. Lett.* **103** 25002

[50] Stenbaek-Nielsen H C, Kanmae T, McHarg M G and Haaland R 2013 High-speed observations of sprite streamers *Surv. Geophys.* **34** 769–95

[51] Nijdam S, Wetering F M V D, Blanc R, Veldhuizen E M V and Ebert U 2010 Probing photo-ionization: experiments on positive streamers in pure gases and mixtures *J. Phys. D: Appl. Phys.* **43** 1

[52] Wang Z, Dijcks S, Guo Y, van der Leegte M, Sun A, Ebert U, Nijdam S and Teunissen J 2023 Quantitative modeling of streamer discharge branching in air *Plasma Sources Sci. Technol.* **32** 1

[53] Briels T M, Kos J, Winands G J, Veldhuizen E M V and Ebert U 2008 Positive and negative streamers in ambient air: measuring diameter, velocity and dissipated energy *J. Phys. D: Appl. Phys.* **41** 234004

[54] Nijdam S, Geurts C G C, van Veldhuizen E M and Ebert U 2009 Reconnection and merging of positive streamers in air *J. Phys. D: Appl. Phys.* **42** 1

[55] Luque A, Ebert U and Hundsdorfer W 2008 Interaction of streamer discharges in air and other oxygen-nitrogen mixtures *Phys. Rev. Lett.* **101** 1

[56] Marskar R Stochastic and self-consistent 3D modeling of streamer discharge trees with kinetic Monte Carlo 2023 (https://doi.org/10.48550/arXiv.2307.01797)

[57] Kotovsky D A and Moore R C 2016 Photochemical response of the nighttime mesosphere to electric field heating - recovery of electron density enhancements *Geophys. Res. Lett.* **43** 952–60

[58] Stenbaek-Nielsen H C, Liu N Y, McHarg M G and Harley J 2023 D region electron density derived from sprite observations *Geophys. Res. Lett.* **50** e2022GL101575